New Journal of Physics

The open access journal at the forefront of physics

PAPER

Sign freedom of non-abelian topological charges in phononic and photonic topological semimetals

Haedong Park and Sang Soon Oh[*]

School of Physics and Astronomy, Cardiff University, Cardiff CF24 3AA, United Kingdom
* Author to whom any correspondence should be addressed.
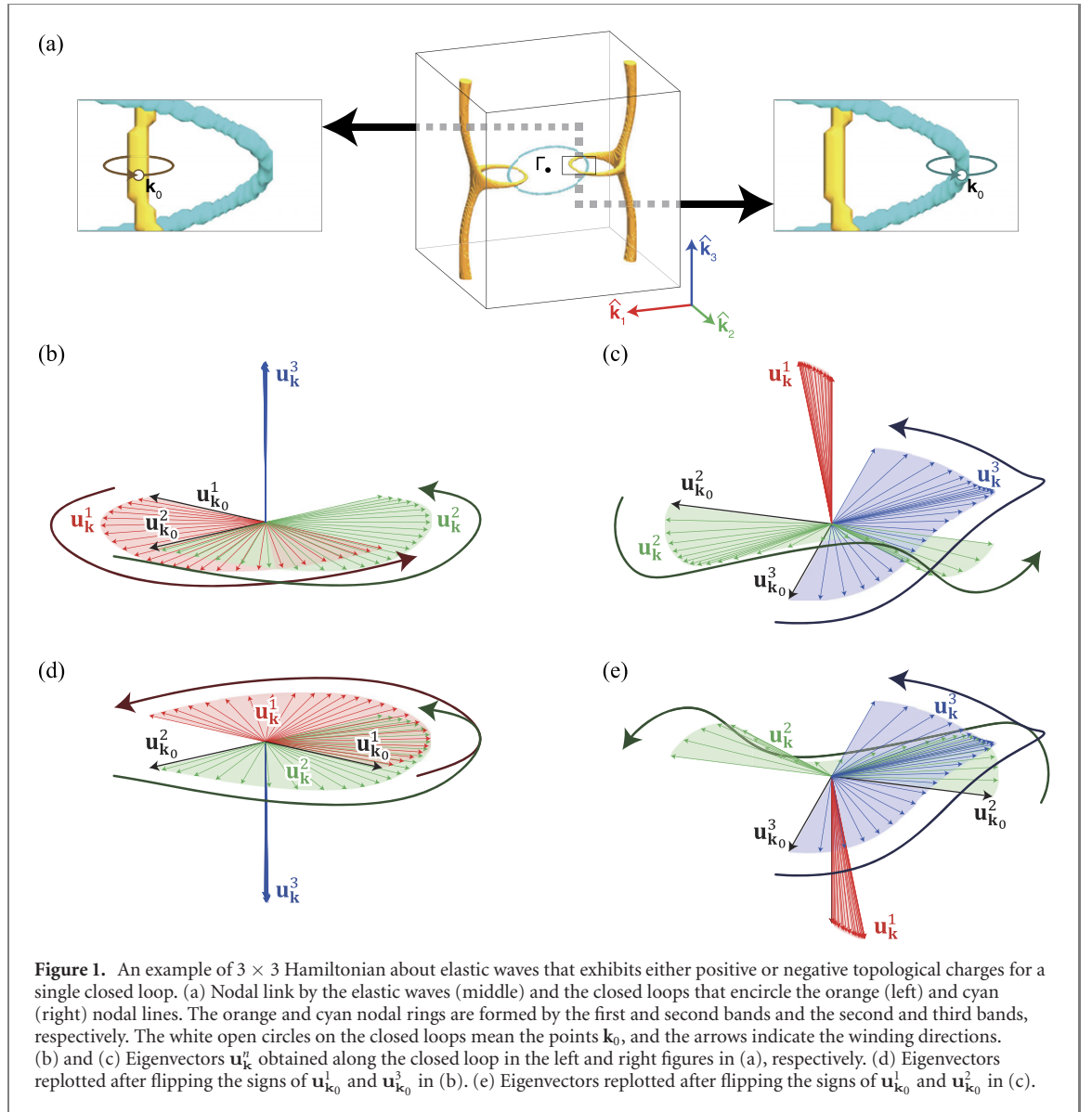
E-mail: ohs2@cardiff.ac.uk

Abstract

The topological nature of nodal lines in three-band systems can be described by non-abelian topological charges called quaternion numbers. Due to the gauge freedom of the eigenstates, the sign of quaternion numbers can be flipped by performing a gauge transformation, i.e., choosing a different basis of eigenstates. However, the sign flipping has not been explicitly shown in realistic systems such as phononic and photonic topological semimetals. Here, we elaborate on the sign freedom of non-abelian topological charges by visualizing numerically calculated topological charges in phononic and photonic topological semimetals. For this, we employ a common reference point method for multiple nodal lines and thus confirm that the sign flipping does not cause any inconsistency in building the quaternion group.

1. Introduction

Multiple nodal lines in momentum space can be interpreted by non-abelian band topology [1]. In particular, topological charges of nodal lines in a three-band system can be described by the quaternion group $\mathbb{Q} = \{\pm i, \pm j, \pm k, \pm 1\}$, where i, j, and k satisfy (i) the square relations $i^2 = j^2 = k^2 = -1$, (ii) the multiplication relations $ij = k$, $jk = i$, $ki = j$, and (iii) anticommutation relations, $ij = -ji$, $jk = -kj$, $ki = -ik$. Recently, a large number of studies on the nodal lines [2–7] have been reported, including nodal rings [8, 9], nodal chains [10–14], nodal links [11, 12, 14–19], and nodal knots [17, 19, 20]. Theoretical and experimental efforts have been made to demonstrate the quaternion topological charges in such nodal line systems [18, 21–24]. Hence, the field of research on the non-abelian topological nodal lines is rapidly expanding in parallel with the study on Dirac [25–32] and Weyl points [33–42].

Although the gauge dependence of the non-abelian charges has been already discussed in the literature [1, 21, 43–47], such property has not been explained by visualizing the eigenstates. In any eigenvalue problem, if $\mathbf{u}$ is an eigenstate of a system, $e^{i\theta}\mathbf{u}$ ($\theta = (0, 2\pi]$) is also an eigenstate of the system, and these two are regarded as the equivalent states (gauge freedom). Even if we restrict the gauge $e^{i\theta}$ to be a real number, i.e., $\theta = 0$ or π, the eigenstate of the system can be expressed either by $\mathbf{u}$ or $-\mathbf{u}$. This means that the gauge freedom allows any signs of the topological charges in the nodal line system generated in the electronic (metals [1, 10, 15] and semimetals [11, 12]), photonic [18, 22], and phononic systems [7, 9, 48]. This property, however, does not contradict the argument of the non-abelian band topology in a three-band system, and it is important to fix the basis of eigenstates as pointed out in reference [1].

In this paper, we elucidate the gauge-dependent sign freedom of the non-abelian topological charges by visualizing the topological charges in phononic and photonic topological semimetals. First, we exemplify such a property with phononic and photonic systems. Then, the reference point method, which is equivalent to fixing of the basis in Hilbert space [1, 45], is adopted for our topological semimetals. Finally, we discuss the consistency of the topological charges' non-abelian relations and the important points to be considered when using this method in phononic and photonic topological semimetals focusing on the path and degeneracies in momentum space.

Figure 1. An example of 3×3 Hamiltonian about elastic waves that exhibits either positive or negative topological charges for a single closed loop. (a) Nodal link by the elastic waves (middle) and the closed loops that encircle the orange (left) and cyan (right) nodal lines. The orange and cyan nodal rings are formed by the first and second bands and the second and third bands, respectively. The white open circles on the closed loops mean the points $\mathbf{k}_0$, and the arrows indicate the winding directions. (b) and (c) Eigenvectors $\mathbf{u}_{\mathbf{k}}^n$ obtained along the closed loop in the left and right figures in (a), respectively. (d) Eigenvectors replotted after flipping the signs of $\mathbf{u}_{\mathbf{k}_0}^1$ and $\mathbf{u}_{\mathbf{k}_0}^3$ in (b). (e) Eigenvectors replotted after flipping the signs of $\mathbf{u}_{\mathbf{k}_0}^1$ and $\mathbf{u}_{\mathbf{k}_0}^2$ in (c).

2. Gauge-dependent property of topological charges

Obtaining the quaternion charge of a nodal line starts with calculating eigenstates along the closed loop that encloses the nodal line. We denote the starting point of the closed loop's winding as $\mathbf{k}_0$ as shown in figure 1(a). Once the signs of the eigenstates at $\mathbf{k}_0$ are determined, their signs at subsequent points $\mathbf{k}$ on the loop are assigned. Finally, the topological charges are calculated by analyzing the rotation behaviors of the eigenstates. Due to the sign freedom of the eigenstates at $\mathbf{k}_0$, the topological charge also has the sign freedom [1, 21, 43–47]. In this section, we discuss the examples that show the sign freedom of the quaternion charges originating from the sign freedom of eigenstates at $\mathbf{k}_0$.

2.1. 3×3 Hamiltonian

We consider phononic waves in an orthotropic elastic material [49] whose constitutive equation is given by Hooke's law $\varepsilon = \mathcal{C} \cdot \mathbf{s}$ (see equation (A.1)). Here, $\varepsilon = \{\varepsilon_{ij}\}$ and $\mathbf{s} = \{s_{ij}\}$ $(i, j = 1, 2, 3)$ are the Cauchy strain and stress tensors, respectively. $\mathcal{C}$ is a compliance matrix, which is a function of Young's moduli, shear moduli and Poisson's ratios: $\mathcal{C} = \mathcal{C}\left(E_i, G_{ij}, \nu_{ij}\right)$. Its inverse is the stiffness matrix $\mathcal{S}$, i.e., $\mathcal{C}^{-1} = \mathcal{S}$, thereby the constitutive equation becomes $\mathbf{s} = \mathcal{S} \cdot \varepsilon$ which is analogous to the one-dimensional Hooke's law $F = -kx$.

By using the density ρ, Young's moduli E_i, shear moduli G_{ij}, Poisson's ratios ν_{ij}, and restoring forces f_i $(i, j = 1, 2, 3)$ listed in table A1 in appendix A, the eigenvalue problem for this elastic wave system is expressed as

$$\begin{bmatrix} H_{11} & H_{12} & H_{13} \\ H_{21} & H_{22} & H_{23} \\ H_{31} & H_{32} & H_{33} \end{bmatrix} \mathbf{u}_{\mathbf{k}}^n = \rho(\omega^n)^2 \mathbf{u}_{\mathbf{k}}^n, \tag{1}$$

with

$$H_{11} = k_1^2 M_{11} + k_2^2 G_{12} + k_3^2 G_{31} + f_1 \tag{1a}$$

$$H_{12} = k_1 k_2 \left(\lambda_{12} + G_{12} \right) \tag{1b}$$

$$H_{13} = k_1 k_3 \left(\lambda_{31} + G_{31} \right) \tag{1c}$$

$$H_{21} = k_1 k_2 \left(\lambda_{12} + G_{12} \right) \tag{1d}$$

$$H_{22} = k_1^2 G_{12} + k_2^2 M_{22} + k_3^2 G_{23} + f_2 \tag{1e}$$

$$H_{23} = k_2 k_3 \left(\lambda_{23} + G_{23} \right) \tag{1f}$$

$$H_{31} = k_1 k_3 \left(\lambda_{31} + G_{31} \right) \tag{1g}$$

$$H_{32} = k_2 k_3 \left(\lambda_{23} + G_{23} \right) \tag{1h}$$

$$H_{33} = k_1^2 G_{31} + k_2^2 G_{23} + k_3^2 M_{33} + f_3, \tag{1i}$$

where $\mathbf{u}_{\mathbf{k}}^n$ ($n = 1, 2, 3$) is the three-component displacement eigenvector satisfying the orthonormal condition $\mathbf{u}_{\mathbf{k}}^m \cdot \mathbf{u}_{\mathbf{k}}^n = \delta^{mn}$, and ω^n is the angular frequency as an eigenfrequency (the detailed derivation of equation (1) can be found in appendix A). Here, the superscript n is the band number, and $\mathbf{k}$ is a point in the momentum space.

For the nodal link shown in figure 1(a) in this phononic system, we choose two closed loops (the arrowed loops) that enclose each nodal ring (the orange and cyan colored shapes, respectively). We calculate the orthonormal eigenvectors $\mathbf{u}_{\mathbf{k}}^n$ along the closed loops [22]. We gather all the eigenstates at the origin, and their evolution in a three-dimensional space $\mathbb{R}^3$ defined by the three components of $\mathbf{u}_{\mathbf{k}}^n$'s are shown in figures 1(b) and (c), respectively. We may regard the topological charge for figure 1(b) as the quaternion number $\boldsymbol{k}$ because $\mathbf{u}_{\mathbf{k}}^1$ and $\mathbf{u}_{\mathbf{k}}^2$ rotate by $+\pi$ around fixed $\mathbf{u}_{\mathbf{k}}^3$ [1, 18, 22, 50]. Likewise, $\mathbf{u}_{\mathbf{k}}^2$ and $\mathbf{u}_{\mathbf{k}}^3$ rotate by $+\pi$ around fixed $\mathbf{u}_{\mathbf{k}}^1$ in figure 1(c), and thereby its topological charge is the quaternion number $\boldsymbol{i}$ [1, 18, 22, 50].

Meanwhile, due to the sign freedom of the eigenstates, we can choose different eigenstates at $\mathbf{k}_0$. For the orange loop in figure 1(a), we flip the signs of $\mathbf{u}_{\mathbf{k}_0}^1$ and $\mathbf{u}_{\mathbf{k}_0}^3$ while keeping $\mathbf{u}_{\mathbf{k}_0}^2$ fixed. Then, $\mathbf{u}_{\mathbf{k}}^n$ at the following points $\mathbf{k}$ on the loop is determined by $\mathbf{u}_{\mathbf{k}_0}^n$. The resulting relation between the eigenstates $\mathbf{u}_{\mathbf{k}}^n$ exhibits $-\pi$-rotations of $\mathbf{u}_{\mathbf{k}}^1$ and $\mathbf{u}_{\mathbf{k}}^2$ around $\mathbf{u}_{\mathbf{k}}^3$ (see figure 1(d)). Thus, the topological charge for this situation is considered as $-\boldsymbol{k}$, compared to figure 1(b). Likewise, we apply the sign-flipping of $\mathbf{u}_{\mathbf{k}_0}^1$ and $\mathbf{u}_{\mathbf{k}_0}^2$ while fixing $\mathbf{u}_{\mathbf{k}_0}^3$ to the cyan loop in figure 1(a). It generates the $-\pi$-rotations of $\mathbf{u}_{\mathbf{k}}^2$ and $\mathbf{u}_{\mathbf{k}}^3$ around $\mathbf{u}_{\mathbf{k}}^1$ (see figure 1(e)) making its topological charge to be $-\boldsymbol{i}$ in contrast to figure 1(c). Therefore, the topological charges of the left and right figures of figure 1(a) can be any of the four sets of quaternion numbers $[\boldsymbol{k}, \boldsymbol{i}]$, $[-\boldsymbol{k}, \boldsymbol{i}]$, $[\boldsymbol{k}, -\boldsymbol{i}]$, or $[-\boldsymbol{k}, -\boldsymbol{i}]$.
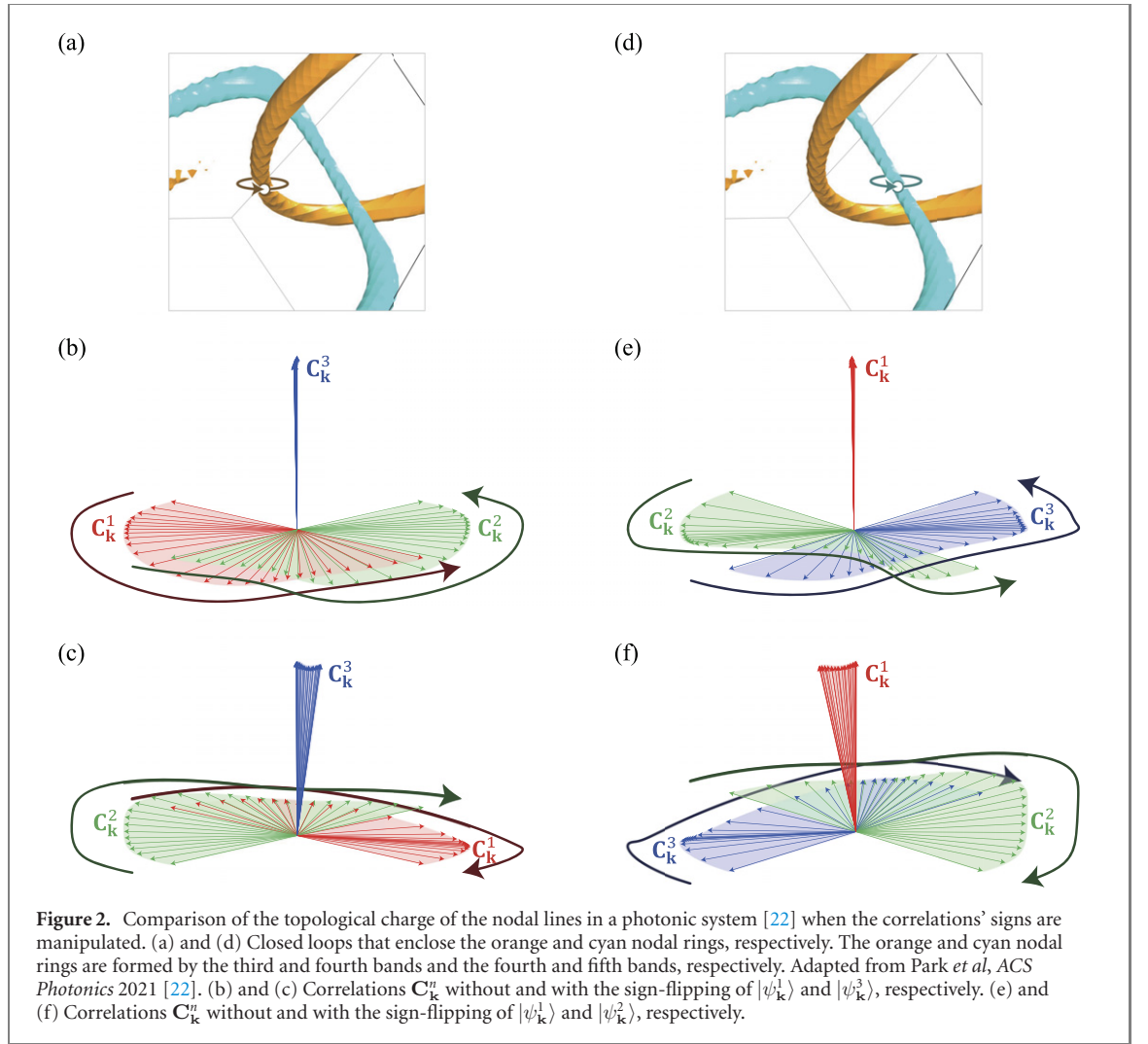
2.2. Correlation vectors in photonic systems

Alternatively, the gauge-dependent non-abelian charges can be visualized using the correlation vectors [22]. For the closed loop in figure 2(a), we compute the orthonormal eigenstates $|\psi_{\mathbf{k}}^n\rangle$ ($n = 1, 2, 3$ for the third, fourth, and fifth bands, respectively). Then, we calculate the correlations $\mathbf{C}_{\mathbf{k}}^n$ defined by the following equation [22]:

$$\mathbf{C}_{\mathbf{k}}^n = \left[\langle \psi_{\mathbf{k}_0}^1 | \psi_{\mathbf{k}}^n \rangle, \langle \psi_{\mathbf{k}_0}^2 | \psi_{\mathbf{k}}^n \rangle, \langle \psi_{\mathbf{k}_0}^3 | \psi_{\mathbf{k}}^n \rangle \right]. \tag{2}$$

All the correlations $\mathbf{C}_{\mathbf{k}}^n$ on the closed loop are collected at the origin, as shown in figure 2(b). The result means its topological charge is $-i\sigma_3$, equivalent to $\boldsymbol{k}$. Now, we adjust the signs of $\left|\psi_{\mathbf{k}_0}^1\right\rangle$ and $\left|\psi_{\mathbf{k}_0}^3\right\rangle$ while fixing the sign of $\left|\psi_{\mathbf{k}_0}^2\right\rangle$. The signs of $|\psi_{\mathbf{k}}^n\rangle$ at the remaining points $\mathbf{k}$ on the closed loop are assigned by the $\left|\psi_{\mathbf{k}_0}^n\right\rangle$. The resulting topological charge in figure 2(c) is $+i\sigma_3$, or $-\boldsymbol{k}$.

Likewise, for the closed loop in figure 2(d), we consider two sets of $\left|\psi_{\mathbf{k}_0}^n\right\rangle$. The sign of $\left|\psi_{\mathbf{k}_0}^n\right\rangle$ in the first set is not adjusted. For the second set, we flip the signs of $\left|\psi_{\mathbf{k}_0}^1\right\rangle$ and $\left|\psi_{\mathbf{k}_0}^2\right\rangle$ with fixing the gauge of $\left|\psi_{\mathbf{k}_0}^3\right\rangle$. Thus, the topological charges of figures 2(e) and (f) are $-i\sigma_1$ and $+i\sigma_1$, respectively, which correspond to $\boldsymbol{i}$ and $-\boldsymbol{i}$, respectively.

Figure 2. Comparison of the topological charge of the nodal lines in a photonic system [22] when the correlations' signs are manipulated. (a) and (d) Closed loops that enclose the orange and cyan nodal rings, respectively. The orange and cyan nodal rings are formed by the third and fourth bands and the fourth and fifth bands, respectively. Adapted from Park *et al*, *ACS Photonics* 2021 [22]. (b) and (c) Correlations $\mathbf{C}_\mathbf{k}^n$ without and with the sign-flipping of $|\psi_\mathbf{k}^1\rangle$ and $|\psi_\mathbf{k}^3\rangle$, respectively. (e) and (f) Correlations $\mathbf{C}_\mathbf{k}^n$ without and with the sign-flipping of $|\psi_\mathbf{k}^1\rangle$ and $|\psi_\mathbf{k}^2\rangle$, respectively.
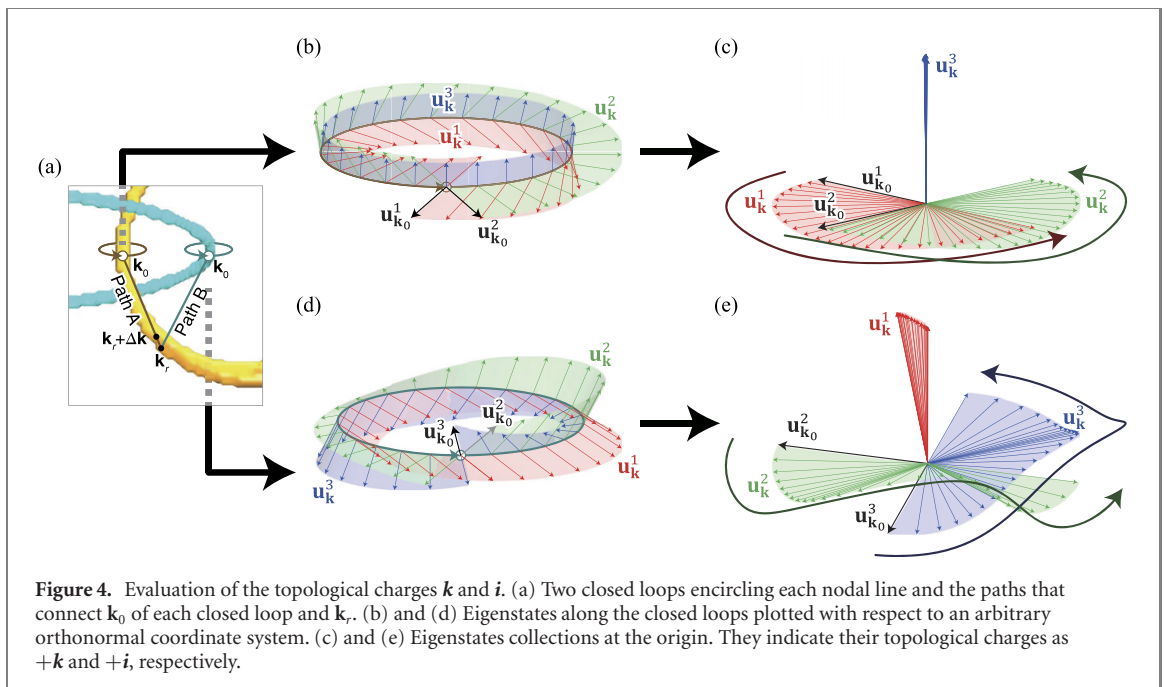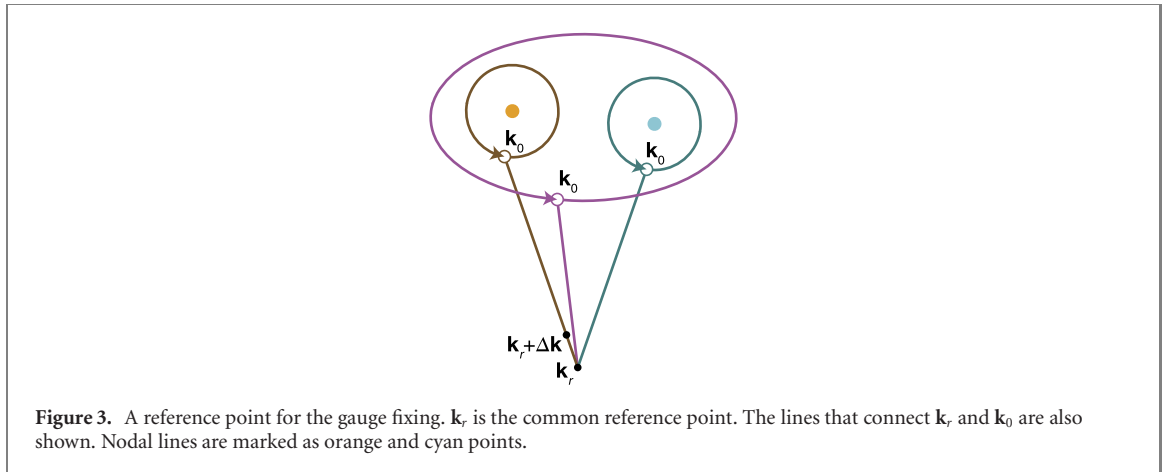
3. Application of common reference point method

To unambiguously determine the signs of the topological charges of our topological semimetals, we fix the gauge of the eigenstates using a reference point [1, 45]. Here, we denote the common reference point as $\mathbf{k}_r$, and a line connects $\mathbf{k}_r$ and $\mathbf{k}_0$ of each loop, as illustrated in figure 3. There can be several $\mathbf{k}_0$ for several closed loops whereas we consider only one $\mathbf{k}_r$. When the topological charge on one closed loop in figure 3 is investigated, $|\psi_{\mathbf{k}_r}^n\rangle$ is calculated first. $|\psi_{\mathbf{k}_r+\Delta\mathbf{k}}^n\rangle$ is also calculated at $\mathbf{k}_r + \Delta\mathbf{k}$ on the $\mathbf{k}_r - \mathbf{k}_0$ line. The sign of $|\psi_{\mathbf{k}_r+\Delta\mathbf{k}}^n\rangle$ is determined to make $\langle\psi_{\mathbf{k}_r}^n|\psi_{\mathbf{k}_r+\Delta\mathbf{k}}^n\rangle$ positive. For all the remaining points $\mathbf{k}$ on the $\mathbf{k}_r - \mathbf{k}_0$ line, the same calculations are performed; the sign of $|\psi_\mathbf{k}^n\rangle$ is determined by $\langle\psi_{\mathbf{k}_r-\Delta\mathbf{k}}^n|\psi_\mathbf{k}^n\rangle > 0$. Once $\mathbf{k}$ reaches $\mathbf{k}_0$, $|\psi_{\mathbf{k}_0}^n\rangle$ is determined. Finally, the topological charge is calculated by the eigenstates only on the loop.

Instead of using the reference point $\mathbf{k}_r$, one can choose the loops whose starting points $\mathbf{k}_0$ coincide at one point in momentum space. However, a smaller loop generates a more accurate topological charge, due to the effect coming from the relative positions between the path and degeneracies that will be explained in section 5.1. Thus, this alternative approach can be employed in limited situations where the nodal lines are sufficiently close to each other.

For the phononic topological semimetals discussed in section 2.1, we set a common reference point $\mathbf{k}_r = [-1, 1, 0.5]$ as shown in figure 4(a), and then we calculated the eigenstates of equation (1) along each path. The eigenstates on the closed loop denoted as path A in figure 4(a) are shown in figure 4(b), and collecting them at the origin results in $+\mathbf{k}$ (as shown in figure 4(c), identical to figure 1(b)). Likewise, the eigenstates on the closed loop denoted as path B in figure 4(a) are plotted in figures 4(d) and (e) (identical to figure 1(c)) resulting in topological charge $+i$. Here, the eigenstates at the common reference point $\mathbf{k}_r$ for path A and B should be identical.

The topological charge $j = ki$ can be described by the composition of the loops in path A and B, which are the closed loops encircling both orange and cyan nodal lines. Note that their starting points $\mathbf{k}_0$ should
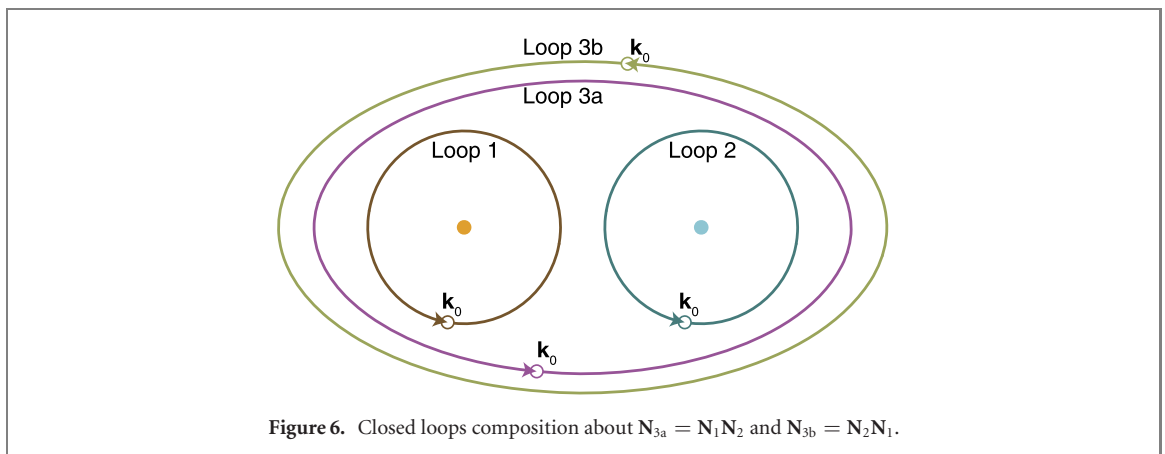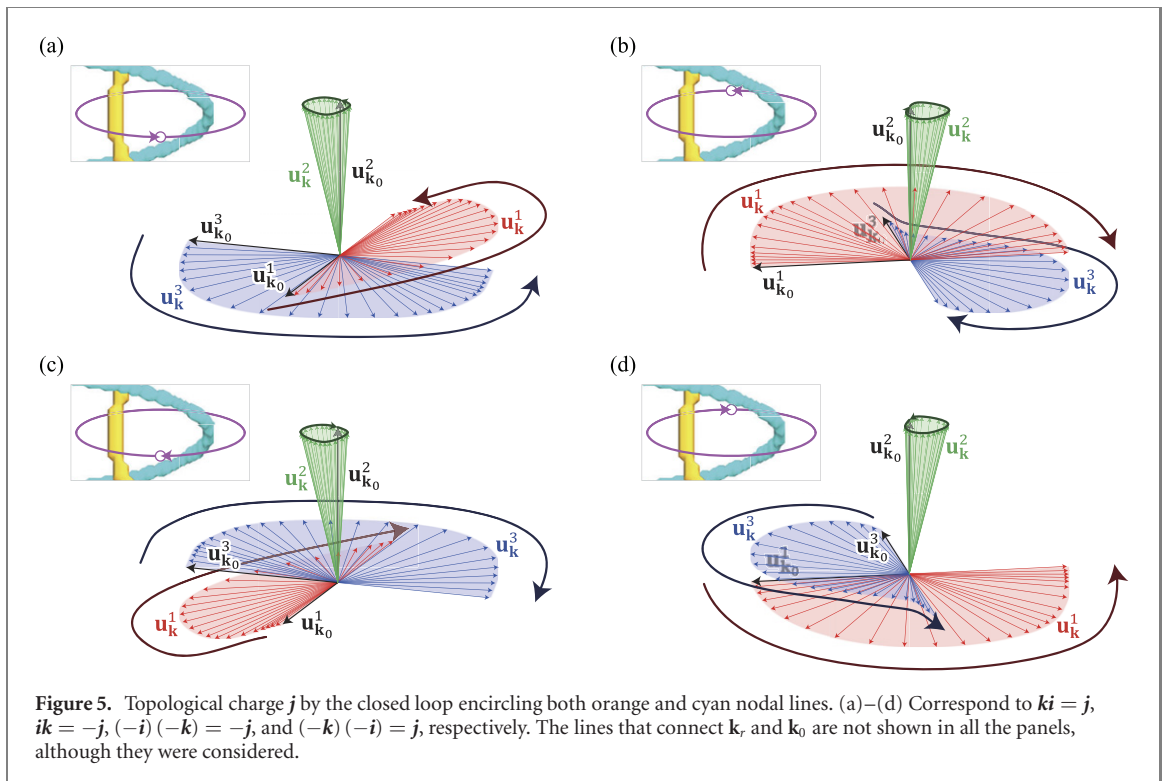
Figure 3. A reference point for the gauge fixing. $\mathbf{k}_r$ is the common reference point. The lines that connect $\mathbf{k}_r$ and $\mathbf{k}_0$ are also shown. Nodal lines are marked as orange and cyan points.

Figure 4. Evaluation of the topological charges $\boldsymbol{k}$ and $\boldsymbol{i}$. (a) Two closed loops encircling each nodal line and the paths that connect $\mathbf{k}_0$ of each closed loop and $\mathbf{k}_r$. (b) and (d) Eigenstates along the closed loops plotted with respect to an arbitrary orthonormal coordinate system. (c) and (e) Eigenstates collections at the origin. They indicate their topological charges as $+\boldsymbol{k}$ and $+\boldsymbol{i}$, respectively.

be connected to the common reference point $\mathbf{k}_r$. Here, the circling sequence is related to the order of $\boldsymbol{k}$ and $\boldsymbol{i}$ in the multiplication. If the first and second half of closed loop scan the cyan ($\boldsymbol{i}$) and orange ($\boldsymbol{k}$) nodal lines, respectively, the relation is written as $\boldsymbol{ki}$. The signs of $\boldsymbol{k}$ and $\boldsymbol{i}$ are concerned with winding direction of the closed loop. As we can consider four different combinations in this multiplication, namely $\boldsymbol{ki}$, $\boldsymbol{ik}$, $(-\boldsymbol{i})(-\boldsymbol{k})$, and $(-\boldsymbol{k})(-\boldsymbol{i})$, their results are $\boldsymbol{j}$, $-\boldsymbol{j}$, $-\boldsymbol{j}$, and $\boldsymbol{j}$ as shown in each panel of figure 5, respectively. The plots in figure 5 are the calibrated results following the step in reference [22]. The calibration angle was set as $0.8\theta_0\,(\mathbf{k})$ where $\theta_0\,(\mathbf{k})$ is the angle between $\mathbf{u}_{\mathbf{k}}^2$ and $\mathbf{u}_{\mathbf{k}_0}^2$.

Note that the topological charges $\boldsymbol{k}$, $\boldsymbol{i}$, and $\pm\boldsymbol{j}$ of the double diamond photonic crystal in reference [22] were calculated using the reference point. More details will be explained in section 5.1.

4. Consistency of topological charges' signs by the reference point method

In the following, we will show that the reference point method can eliminate the chance that the non-abelian charges are misinterpreted as abelian. For example, let us suppose that two closed loops, which are marked as loop 1 and 2 in figure 6, respectively, are in different locations in momentum space. If we denote topological charges by these loops as $\mathbf{N}_1$ and $\mathbf{N}_2$, respectively, and if we consider an additional loop, marked as loop 3a in figure 6, circling along loop 2 and 1 in sequence [18, 22], the loop 3a's topological charge $\mathbf{N}_{3a}$ is calculated by the composition of $\mathbf{N}_1$ and $\mathbf{N}_2$, i.e., $\mathbf{N}_{3a} = \mathbf{N}_1\mathbf{N}_2$. We also suppose that loop 3b scans around loop 1 first then circles along loop 2, as shown in figure 6. Its topological charge is expressed as $\mathbf{N}_{3b} = \mathbf{N}_2\mathbf{N}_1$. If $\mathbf{N}_{3a}$ and $\mathbf{N}_{3b}$ satisfy $\mathbf{N}_{3a} = -\mathbf{N}_{3b}$, this leads to $\mathbf{N}_1\mathbf{N}_2 = -\mathbf{N}_2\mathbf{N}_1$. This relation can be called
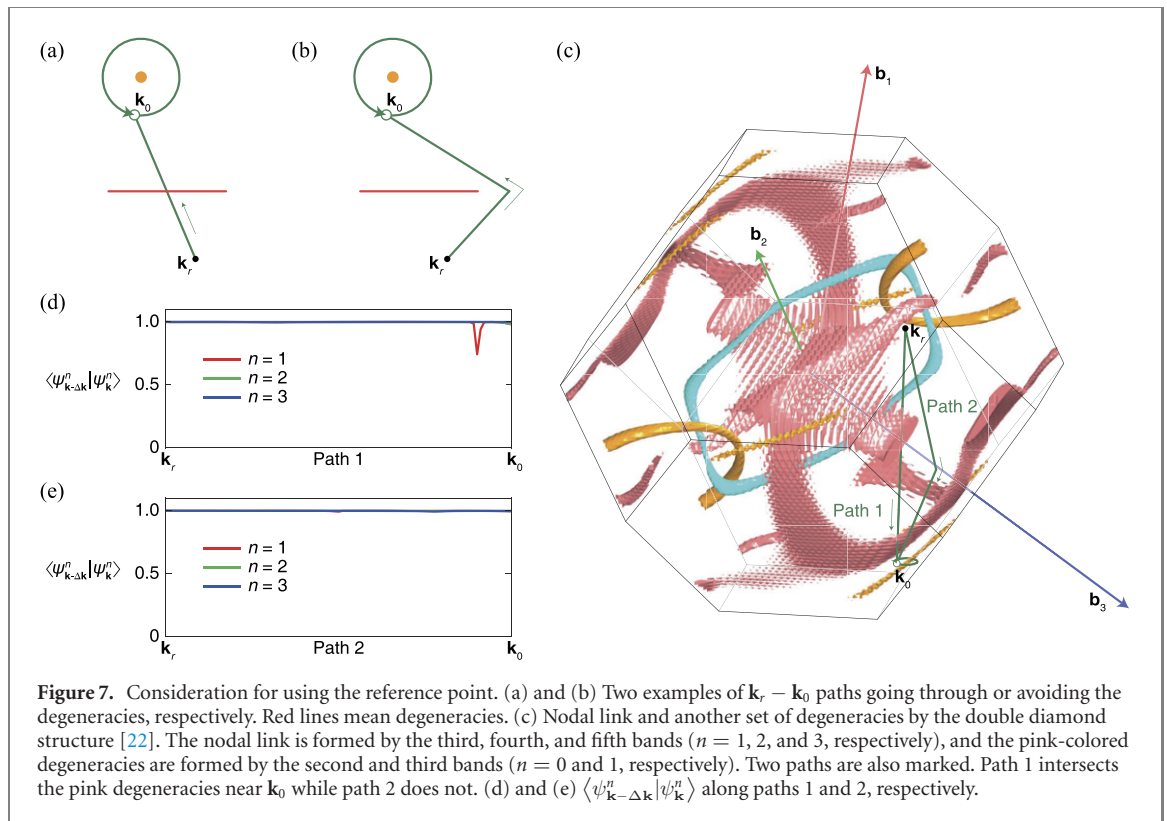
Figure 5. Topological charge j by the closed loop encircling both orange and cyan nodal lines. (a)–(d) Correspond to $ki = j$, $ik = -j$, $(-i)(-k) = -j$, and $(-k)(-i) = j$, respectively. The lines that connect $\mathbf{k}_r$ and $\mathbf{k}_0$ are not shown in all the panels, although they were considered.

Figure 6. Closed loops composition about $\mathbf{N}_{3a} = \mathbf{N}_1\mathbf{N}_2$ and $\mathbf{N}_{3b} = \mathbf{N}_2\mathbf{N}_1$.

'non-abelian'. To write this relation, the signs of each charge should be first determined by such kind of sign convention. If there is not any sign convention, and if the topological charge of loop 3b can be either plus or minus, it means that we can assume the sign-flipping of $\mathbf{N}_{3b}$ while fixing the other charges' signs. Then, the above relation $\mathbf{N}_{3a} = -\mathbf{N}_{3b}$ becomes $\mathbf{N}_{3a} = \mathbf{N}_{3b}$ or $\mathbf{N}_1\mathbf{N}_2 = \mathbf{N}_2\mathbf{N}_1$. Thus, such a situation could be incorrectly interpreted as 'abelian'. This behavior is, however, simply a result coming from the gauge freedom of the eigenstates, and there is no inconsistency in the non-abelian nature of the non-abelian band topology.

5. Remaining issues when using the reference point method in phononic and photonic topological semimetals

5.1. $\mathbf{k}_r - \mathbf{k}_0$ path and degeneracies

Although figure 3 illustrates the paths between $\mathbf{k}_r$ and $\mathbf{k}_0$ as a line, they do not have to be a straight line. Instead of the straight line (see figure 7(a)), the path sometimes should make a detour around degeneracies (see figure 7(b)) which can be zero-, one-, two-, or three-dimensional. Let us suppose we investigate the topological nature of three bands indexed as n, $n + 1$, and $n + 2$. Then, the paths should avoid the degeneracies that at least one of the three bands is concerned with, e.g., the degeneracies by the bands $n - 1$ and n or the degeneracies by the bands $n + 2$ and $n + 3$. This is because the degeneracies destroy the

Figure 7. Consideration for using the reference point. (a) and (b) Two examples of $\mathbf{k}_r - \mathbf{k}_0$ paths going through or avoiding the degeneracies, respectively. Red lines mean degeneracies. (c) Nodal link and another set of degeneracies by the double diamond structure [22]. The nodal link is formed by the third, fourth, and fifth bands ($n = 1, 2$, and 3, respectively), and the pink-colored degeneracies are formed by the second and third bands ($n = 0$ and 1, respectively). Two paths are also marked. Path 1 intersects the pink degeneracies near $\mathbf{k}_0$ while path 2 does not. (d) and (e) $\langle \psi_{\mathbf{k}-\Delta\mathbf{k}}^n | \psi_{\mathbf{k}}^n \rangle$ along paths 1 and 2, respectively.

eigenstates information at $\mathbf{k}_r$. In figure 7(c), path 1 goes through the pink points (near $\mathbf{k}_0$) while path 2 avoids them. The pink points are degeneracies between the second and third bands ($n = 0$ and 1, respectively). $\langle \psi_{\mathbf{k}-\Delta\mathbf{k}}^n | \psi_{\mathbf{k}}^n \rangle$ ($n = 1, 2, 3$) at each point on path 1 are calculated, and only the value with $n = 1$ shows the sharp change around the degeneracies (see figure 7(d)). In contrast, their behaviors on path 2 do not exhibit such a sharp change (see figure 7(e)). In other words, the eigenstates information at $\mathbf{k}_r$ cannot be delivered through the degeneracies because the degeneracies may act as the sink or source of certain topological states, like Weyl points [33–42, 51, 52].

Importantly, the sign of the quaternion charges depends on which detour the path takes, as discussed in references [1, 45]. In our elastic system, we considered $\mathbf{k}_r$ located in front of the nodal link, as shown in figure 4(a). When the same reference point is used to figure 5, multiple detour options are available for setting $\mathbf{k}_r - \mathbf{k}_0$ in figures 5(b) and (d), unlike the points $\mathbf{k}_0$ in figures 5(a) and (c) that can be connected to $\mathbf{k}_r$ along the shortest path. To calculate the topological charges in figures 5(b) and (d), we used straight $\mathbf{k}_r - \mathbf{k}_0$ passing the center of the insets in figures 5(b) and (d). These paths go through both orange and cyan rings. If we choose a detour $\mathbf{k}_r - \mathbf{k}_0$ that does not pass through any of these rings, the signs of the topological charges in figures 5(b) and (d) remain the same. If the path pierces through only one ring, the signs are flipped, which can be analyzed in depth following references [1, 45].

Based on the above discussion, it is desirable to set the reference point $\mathbf{k}_r$ that makes the overall $\mathbf{k}_r - \mathbf{k}_0$ short as possible to reduce the chance of losing the Bloch states' gauge information. Especially, at the first step of calculating the quaternion charges, it is simple to set the $\mathbf{k}_r - \mathbf{k}_0$ not to pass through nodal rings. If $\mathbf{k}_r$ and $\mathbf{k}_0$ are in opposite regions of degeneracies, the topological charge's signs should be examined using references [1, 45].

5.2. Gauge freedom at the reference point

Although we have examined the topological charges of our topological semimetals using the reference point method, the exact sign on each topological charge is not fully determined due to the sign freedom of the eigenstates at $\mathbf{k}_r$. If the eigenstates' signs at $\mathbf{k}_r$ are flipped, some quaternion charges' signs may be flipped while the other quaternion charges' signs do not change. For example, regarding figures 4 and 5, if we flip the signs of $\mathbf{u}_{\mathbf{k}_r}^1$ and $\mathbf{u}_{\mathbf{k}_r}^2$ at $\mathbf{k}_r$, the result in figure 4(e) may change from $\boldsymbol{i}$ to $-\boldsymbol{i}$ while the topological charge of figure 4(c) is still $\boldsymbol{k}$. In this case, the anticommutative relations between the charges are still valid as the signs in figure 5 are also reversed.

6. Conclusions

In summary, we have shown that the sign of quaternion charges can be flipped due to the gauge freedom of eigenstates by using the phononic and photonic topological semimetals. We have also applied the reference point method, which is equivalent to the basis fixing, to our topological semimetals. Additionally, the consistency of non-abelian relationship between topological charges with this method has been discussed.

Based on the discussions in section 5.2, we make the following conclusions: (i) gauge fixing by a common reference point does not result in unique signs of the quaternion charges' signs but makes the non-abelian relations satisfied by the quaternion charges, (ii) the signs of nodal lines can be flipped by choosing the eigenstates' signs at a reference point $\mathbf{k}_r$. In other words, the sign relation between different nodal lines is more important than the absolute sign of quaternion charges corresponding to each loop.

Acknowledgments

Data availability statement

The data that support the findings of this study are available upon reasonable request from the authors.

Appendix A. Derivation of 3 × 3 Hamiltonian for an orthotropic elastic material

The constitutive equation for an orthotropic elastic material is expressed as $\varepsilon = \mathcal{C} \cdot \mathbf{s}$, or

$$
\begin{bmatrix} \varepsilon_{11} \\ \varepsilon_{22} \\ \varepsilon_{33} \\ 2\varepsilon_{23} \\ 2\varepsilon_{31} \\ 2\varepsilon_{12} \end{bmatrix} = \mathcal{C} \cdot \begin{bmatrix} s_{11} \\ s_{22} \\ s_{33} \\ s_{23} \\ s_{31} \\ s_{12} \end{bmatrix}, \tag{A.1}
$$

where $\varepsilon = \{\varepsilon_{ij}\}$ and $\mathbf{s} = \{s_{ij}\}$ are the Cauchy strain and stress tensors, respectively ($i, j = 1, 2, 3$). Each component of the Cauchy strain tensor is expressed as $\varepsilon_{ij} = (1/2)(\partial u_i/\partial X_j + \partial u_j/\partial X_i)$ where $\mathbf{u} = [u_1, u_2, u_3]$ is the displacement vector. $\mathcal{C}$ is the compliance tensor:
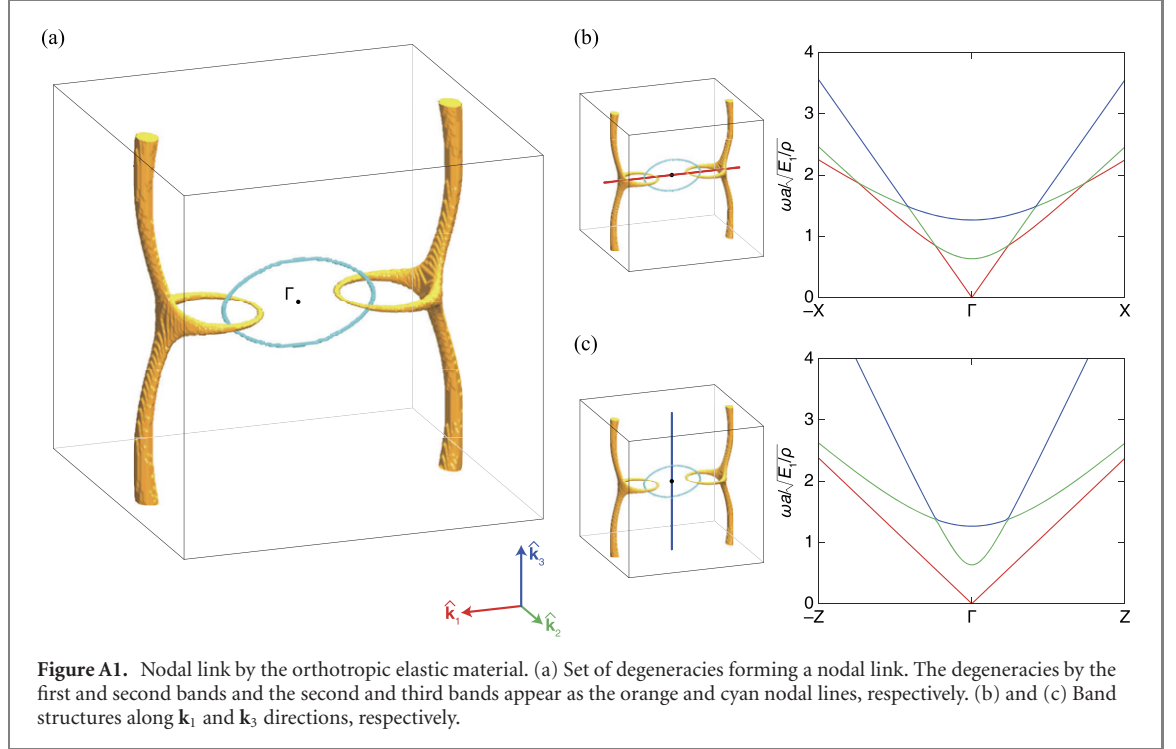
$$
\mathcal{C} = \begin{bmatrix} \dfrac{1}{E_1} & -\dfrac{\nu_{21}}{E_2} & -\dfrac{\nu_{31}}{E_3} & 0 & 0 & 0 \\[2mm] -\dfrac{\nu_{12}}{E_1} & \dfrac{1}{E_2} & -\dfrac{\nu_{32}}{E_3} & 0 & 0 & 0 \\[2mm] -\dfrac{\nu_{13}}{E_1} & -\dfrac{\nu_{23}}{E_2} & \dfrac{1}{E_3} & 0 & 0 & 0 \\[2mm] 0 & 0 & 0 & \dfrac{1}{G_{23}} & 0 & 0 \\[2mm] 0 & 0 & 0 & 0 & \dfrac{1}{G_{31}} & 0 \\[2mm] 0 & 0 & 0 & 0 & 0 & \dfrac{1}{G_{12}} \end{bmatrix}, \tag{A.2}
$$

where E_i is the Young's modulus along i-direction and $G_{ij} = G_{ji}$ is the shear modulus along i-direction on the plane normal to j-direction. ν_{ij} is the Poisson's ratio, the negative ratio of a transverse strain along j-direction to a longitudinal strain along i-direction. Because we assume an orthotropic material, the relation $\nu_{ij}/E_i = \nu_{ji}/E_j$ holds and the compliance tensor $\mathcal{C}$ is symmetric.

The wave equation for an elastic material is $-\nabla \cdot \mathbf{s} - \mathbf{F}_v = -\rho \ddot{\mathbf{u}}$, where $\mathbf{F}_v$ is the body force. Here, we consider the body force as the restoring force expressed as $\mathbf{F}_v = -\mathbf{f} \cdot \mathbf{u}$, i.e., $\mathbf{F}_v = -[f_1 u_1, f_2 u_2, f_3 u_3]$. If the displacement vector is expressed as $\mathbf{u}(\mathbf{x}, t) = \mathbf{u}(\mathbf{x}) \exp(-i\omega t) = \mathbf{u_k} \exp(-i\mathbf{k} \cdot \mathbf{x}) \exp(-i\omega t)$, substituting this into the wave equation leads equation (1). In equation (1), M_{ii} and λ_{ij} are the components of the

Table A1. Parameter-sets to realize the nodal links by orthotropic elastic material.

Quantities	Values
Young's moduli (MPa)	$E_1 = 50, E_2 = 40, E_3 = 110$
Shear moduli (MPa)	$G_{12} = 17.5, G_{23} = 26.7, G_{31} = 28.6$
Poisson's ratios (1)	$\nu_{21} = 0.25, \nu_{13} = 0.2, \nu_{32} = 0.4$
Density (kg m^{-3})	$\rho = 1000$
Restoring forces (N m^{-3})	$f_1 = 0, f_2 = 80, f_3 = 20$

Figure A1. Nodal link by the orthotropic elastic material. (a) Set of degeneracies forming a nodal link. The degeneracies by the first and second bands and the second and third bands appear as the orange and cyan nodal lines, respectively. (b) and (c) Band structures along $\mathbf{k}_1$ and $\mathbf{k}_3$ directions, respectively.

stiffness matrix $\mathcal{S} = \mathcal{C}^{-1}$ as follows:

$$
\mathcal{S} = \begin{bmatrix}
M_{11} & \lambda_{21} & \lambda_{31} & 0 & 0 & 0 \\
\lambda_{12} & M_{22} & \lambda_{23} & 0 & 0 & 0 \\
\lambda_{31} & \lambda_{23} & M_{33} & 0 & 0 & 0 \\
0 & 0 & 0 & G_{23} & 0 & 0 \\
0 & 0 & 0 & 0 & G_{31} & 0 \\
0 & 0 & 0 & 0 & 0 & G_{12}
\end{bmatrix}. \tag{A.3}
$$

This orthotropic elastic material forms a nodal link when the parameters in table A1 are used. In the given the momentum space with $-\pi \leqslant k_1 \leqslant \pi$, $-\pi \leqslant k_2 \leqslant \pi$, and $-\pi \leqslant k_3 \leqslant \pi$, we calculated the eigenfrequencies ω^n. We regarded that two bands n and $n + 1$ at point $\mathbf{k}$ are degenerate if $\left| \omega^{n+1} - \omega^n \right| a / \sqrt{E_1/\rho} < 0.0268$, where $a = 1$ m is the constant for normalization. Sets of the degeneracies formed between the first and second bands and the second and third bands are depicted as orange and cyan nodal lines, respectively, in figure A1(a). Band structures along $\mathbf{k}_1$ and $\mathbf{k}_3$ directions are also given in figures A1(b) and (c), respectively.

ORCID iDs

Sang Soon Oh   https://orcid.org/0000-0003-3093-7016

References

[1] Wu Q, Soluyanov A A and Bzdušek T 2019 Non-abelian band topology in noninteracting metals *Science* **365** 1273–7

[2] Ahn J, Kim D, Kim Y and Yang B J 2018 Band topology and linking structure of nodal line semimetals with Z_2 monopole charges *Phys. Rev. Lett.* **121** 106403

[3] Bouhon A, Wu Q, Slager R J, Weng H, Yazyev O V and Bzdušek T 2020 Non-abelian reciprocal braiding of Weyl points and its manifestation in ZrTe *Nat. Phys.* **16** 1137–43

[4] Xia L, Guo Q, Yang B, Han J, Liu C X, Zhang W and Zhang S 2019 Observation of hourglass nodal lines in photonics *Phys. Rev. Lett.* **122** 103903

[5] Kim M, Jacob Z and Rho J 2020 Recent advances in 2D, 3D and higher-order topological photonics *Light: Sci. Appl.* **9** 130

[6] Lenggenhager P M, Liu X, Tsirkin S S, Neupert T and Bzdušek T 2021 From triple-point materials to multiband nodal links *Phys. Rev. B* **103** L121101

[7] Park S, Hwang Y, Choi H C and Yang B J 2021 Topological acoustic triple point *Nat. Commun.* **12** 6781

[8] Gao W, Yang B, Tremain B, Liu H, Guo Q, Xia L, Hibbins A P and Zhang S 2018 Experimental observation of photonic nodal line degeneracies in metacrystals *Nat. Commun.* **9** 950

[9] Deng W, Lu J, Li F, Huang X, Yan M, Ma J and Liu Z 2019 Nodal rings and drumhead surface states in phononic crystals *Nat. Commun.* **10** 1769

[10] Bzdušek T, Wu Q, Rüegg A, Sigrist M and Soluyanov A A 2016 Nodal-chain metals *Nature* **538** 75–8

[11] Chang G *et al* 2017 Topological Hopf and chain link semimetal states and their application to Co_2MnGa *Phys. Rev. Lett.* **119** 156401

[12] Yan Z, Bi R, Shen H, Lu L, Zhang S C and Wang Z 2017 Nodal-link semimetals *Phys. Rev. B* **96** 041103

[13] Yan Q, Liu R, Yan Z, Liu B, Chen H, Wang Z and Lu L 2018 Experimental discovery of nodal chains *Nat. Phys.* **14** 461–4

[14] Belopolski I *et al* 2019 Discovery of topological Weyl fermion lines and drumhead surface states in a room temperature magnet *Science* **365** 1278–81

[15] Xie Y, Cai J, Kim J, Chang P Y and Chen Y 2019 Hopf-chain networks evolved from triple points *Phys. Rev. B* **99** 165147

[16] He P, Fu J H, Zhang D W and Zhu S L 2020 Double exceptional links in a three-dimensional dissipative cold atomic gas *Phys. Rev. A* **102** 023308

[17] Lee C H *et al* 2020 Imaging nodal knots in momentum space through topolectrical circuits *Nat. Commun.* **11** 4385

[18] Yang E *et al* 2020 Observation of non-abelian nodal links in photonics *Phys. Rev. Lett.* **125** 033901

[19] Yang Z, Chiu C K, Fang C and Hu J 2020 Jones polynomial and knot transitions in Hermitian and non-Hermitian topological semimetals *Phys. Rev. Lett.* **124** 186402

[20] Bi R, Yan Z, Lu L and Wang Z 2017 Nodal-knot semimetals *Phys. Rev. B* **96** 201305

[21] Guo Q, Jiang T, Zhang R Y, Zhang L, Zhang Z Q, Yang B, Zhang S and Chan C T 2021 Experimental observation of non-abelian topological charges and edge states *Nature* **594** 195–200

[22] Park H, Wong S, Zhang X and Oh S S 2021 Non-abelian charged nodal links in a dielectric photonic crystal *ACS Photonics* **8** 2746–54

[23] Wang D *et al* 2021 Intrinsic in-plane nodal chain and generalized quaternion charge protected nodal link in photonics *Light: Sci. Appl.* **10** 83

[24] Yang B *et al* 2021 Momentum space toroidal moment in a photonic metamaterial *Nat. Commun.* **12** 1784

[25] Lu L, Fang C, Fu L, Johnson S G, Joannopoulos J D and Soljačić M 2016 Symmetry-protected topological photonic crystal in three dimensions *Nat. Phys.* **12** 337–40

[26] Abbaszadeh H, Souslov A, Paulose J, Schomerus H and Vitelli V 2017 Sonic Landau levels and synthetic gauge fields in mechanical metamaterials *Phys. Rev. Lett.* **119** 195502

[27] Brendel C, Peano V, Painter O J and Marquardt F 2017 Pseudomagnetic fields for sound at the nanoscale *Proc. Natl Acad. Sci. USA* **114** E3390–5

[28] Jin D, Christensen T, Soljačić M, Fang N X, Lu L and Zhang X 2017 Infrared topological plasmons in graphene *Phys. Rev. Lett.* **118** 245301

[29] Slobozhanyuk A, Mousavi S H, Ni X, Smirnova D, Kivshar Y S and Khanikaev A B 2017 Three-dimensional all-dielectric photonic topological insulator *Nat. Photon.* **11** 130–6

[30] Liu G G *et al* 2020 Observation of an unpaired photonic Dirac point *Nat. Commun.* **11** 1873

[31] Wang P, Lu L and Bertoldi K 2015 Topological phononic crystals with one-way elastic edge waves *Phys. Rev. Lett.* **115** 104302

[32] Wen X, Qiu C, Qi Y, Ye L, Ke M, Zhang F and Liu Z 2019 Acoustic Landau quantization and quantum-Hall-like edge states *Nat. Phys.* **15** 352–6

[33] Lu L, Fu L, Joannopoulos J D and Soljačić M 2013 Weyl points and line nodes in gyroid photonic crystals *Nat. Photon.* **7** 294

[34] Lu L, Wang Z, Ye D, Ran L, Fu L, Joannopoulos J D and Soljačić M 2015 Experimental observation of Weyl points *Science* **349** 622–4

[35] Soluyanov A A, Gresch D, Wang Z, Wu Q, Troyer M, Dai X and Bernevig B A 2015 Type-II Weyl semimetals *Nature* **527** 495

[36] He H, Qiu C, Ye L, Cai X, Fan X, Ke M, Zhang F and Liu Z 2018 Topological negative refraction of surface acoustic waves in a Weyl phononic crystal *Nature* **560** 61–4

[37] Yang B *et al* 2018 Ideal Weyl points and helicoid surface states in artificial photonic crystal structures *Science* **359** 1013–6

[38] Jia H *et al* 2019 Observation of chiral zero mode in inhomogeneous three-dimensional Weyl metamaterials *Science* **363** 148–51

[39] Peri V, Serra-Garcia M, Ilan R and Huber S D 2019 Axial-field-induced chiral channels in an acoustic Weyl system *Nat. Phys.* **15** 357–61

[40] Yang Y, Xia J p, Sun H x, Ge Y, Jia D, Yuan S q, Yang S A, Chong Y and Zhang B 2019 Observation of a topological nodal surface and its surface-state arcs in an artificial acoustic crystal *Nat. Commun.* **10** 5185

[41] He H, Qiu C, Cai X, Xiao M, Ke M, Zhang F and Liu Z 2020 Observation of quadratic Weyl points and double-helicoid arcs *Nat. Commun.* **11** 1820

[42] Park H and Lee S 2020 Double gyroids for frequency-isolated Weyl points in the visible regime and interference lithographic design *ACS Photonics* **7** 1577–85

[43] Bouhon A, Black-Schaffer A M and Slager R J 2019 Wilson loop approach to fragile topology of split elementary band representations and topological crystalline insulators with time-reversal symmetry *Phys. Rev. B* **100** 195135

[44] Bouhon A, Bzdušek T and Slager R J 2020 Geometric approach to fragile topology beyond symmetry indicators *Phys. Rev. B* **102** 115135

[45] Tiwari A and Bzdušek T 2020 Non-abelian topology of nodal-line rings in $\mathcal{PT}$-symmetric systems *Phys. Rev. B* **101** 195130

[46] Jiang B, Bouhon A, Lin Z K, Zhou X, Hou B, Li F, Slager R J and Jiang J H 2021 Experimental observation of non-abelian topological acoustic semimetals and their phase transitions *Nat. Phys.* **17** 1239–46

[47] Peng B, Bouhon A, Monserrat B and Slager R J 2022 Phonons as a platform for non-abelian braiding and its manifestation in layered silicates *Nat. Commun.* **13** 423

[48] Merkel A and Christensen J 2019 Ultrasonic nodal chains in topological granular metamaterials *Commun. Phys.* **2** 154

[49] Beer F P, Russell Johnston E, DeWolf J T and Mazurek D F 2012 *Mechanics of Materials* (New York: McGraw-Hill)

[50] Park H, Gao W, Zhang X and Oh S S 2022 Nodal lines in momentum space: topological invariants and recent realizations in photonic and other systems *Nanophotonics* (https://doi.org/10.1515/nanoph-2021-0692)

[51] Fruchart M, Jeon S Y, Hur K, Cheianov V, Wiesner U and Vitelli V 2018 Soft self-assembly of Weyl materials for light and sound *Proc. Natl Acad. Sci. USA* **115** E3655–64

[52] Yang Z, Xiao M, Gao F, Lu L, Chong Y and Zhang B 2017 Weyl points in a magnetic tetrahedral photonic crystal *Opt. Express* **25** 15772–7